Sensors & Diagnostics

PAPER

View Article Online
View Journal | View Issue

Cite this: *Sens. Diagn.*, 2023, **2**, 1249

Photoelectrochemical immunoassay of alpha-fetoprotein based on a SnO_2/In_2S_3 heterojunction and an enzyme-catalyzed precipitation strategy†

Lu Li, Yaqing Weng, Chenglong Sun, Yueyi Peng * and Qingji Xie *

Received 5th May 2023,
Accepted 28th June 2023

DOI: 10.1039/d3sd00105a

rsc.li/sensors

We report the sensitive photoelectrochemical (PEC) sandwich-type immunosensing of alpha-fetoprotein (AFP) by using SnO_2/In_2S_3 as a novel heterojunction material and horseradish peroxidase (HRP)–CeO_2 as an efficient biolabel. A SnO_2/In_2S_3/fluorine-doped tin oxide (FTO) photoanode was fabricated by hydrothermally synthesizing SnO_2/In_2S_3 and cast-coating it on a FTO slice. A HRP–CeO_2–secondary antibody–bovine serum albumin complex was immunologically immobilized on the photoanode, and the PEC immunoassay of AFP was realized by the HRP and mimetic enzyme CeO_2 catalyzed oxidation of 3-amino-9-ethylcarbazole by H_2O_2 to generate a precipitate with a steric hindrance effect. Under optimized conditions, the value of photocurrent decrease was linear with the common logarithm of AFP concentration from 500 fg mL^{-1} to 50 ng mL^{-1}, and the limit of detection (S/N = 3) is 0.15 pg mL^{-1}.

Introduction

Liver cancer is one of the deadliest diseases worldwide, accounting for 8.3% of all cancer deaths.[1,2] Alpha-fetoprotein (AFP) is an important biomarker for early diagnosis, efficacy evaluation, postoperative monitoring, and long-term evaluation of liver cancer.[3] Serum AFP levels are usually lower than 25 ng mL^{-1} in healthy adults, but are notably higher in patients with liver cancer and continue to increase with the disease progress.[4] To date, many analytical methods have been established for AFP assay, such as enzyme-linked immunosorbent assay,[5] electrochemiluminescence immunoassay,[6] fluorescence assay,[7] and electrochemical assay,[8] each with its advantages and disadvantages. Obviously, it is an interesting and important topic to develop simple, accurate and sensitive analytical methods for AFP assays.

Photoelectrochemical (PEC) analysis has the advantages of low background and high sensitivity due to separation of the excitation source and output signal.[9–11] PEC analysis performance relies heavily on the PEC materials, which can be used both as light-harvesting substances to generate PEC signals and as substrates to immobilize biomolecules. Many metal oxides, metal sulfides, quantum dots, and metal–organic frameworks have been widely used due to their excellent PEC properties. Among them, SnO_2 (E_g ~ 3.6 eV) is a typical metal oxide semiconductor exhibiting high ultraviolet absorption, high stability and environmental friendliness.[12,13] The wide bandgap of SnO_2 limits its ability to absorb only ultraviolet light and it has a high electron–hole recombination degree, but the PEC performance can be improved by heterojunction formation, doping, sensitization, and noble metal loading.[14] In_2S_3 (E_g ~ 2.0 eV) is a narrow band gap n-type semiconductor with high photoactivity and is promising for photocatalysis, CO_2 reduction and solar cell applications.[15–17] As far as we know, construction and application of SnO_2/In_2S_3 heterojunctions in the PEC field have not been reported.

Signal output and amplification strategies also play a key role in determining the sensitivity and selectivity of a PEC biosensor.[18] To date, steric hindrance effects, energy transfer principles, p–n semiconductor quenching effects and enzymatic reactions have been widely used to output and amplify PEC signals.[19,20] The catalyzed precipitation (CP) reaction can be used to quench the photocurrent signal by generating insoluble precipitates with a steric hindrance effect on the electrode surface and thus give obvious response signals and high sensitivity.[21] CP based on natural enzymes such as horseradish peroxidase (HRP) and alkaline phosphate (ALP) has been reported.[19,22] On the other hand, nanozymes (nanomaterials with enzyme-like properties) have also been widely used because of their good stability and low cost. CeO_2 has received extensive attention in the fields of photocatalysis and biosensor due to its favorable electrical, optical and peroxidase-like properties.[23] Here, CeO_2 of a uniform nanocube structure

Key Laboratory of Chemical Biology & Traditional Chinese Medicine Research (Ministry of Education of China), College of Chemistry and Chemical Engineering, Hunan Normal University, Changsha 410081, China.
E-mail: pengyueyi@hunnu.edu.cn, xieqj@hunnu.edu.cn

† Electronic supplementary information (ESI) available. See DOI: https://doi.org/10.1039/d3sd00105a

is employed as a secondary antibody (Ab_2) label, because it can act as both an excellent carrier for loading biomolecules and a peroxidase-like nanozyme to catalyze precipitation together with the natural enzyme HRP. As far as we know, Ab_2 labeling with a CeO_2 nanozyme and HRP natural enzyme to catalyze the production of an insoluble precipitate on the photoelectrode surface for signaling in a PEC AFP immunoassay has not been reported to date.

Herein, we hydrothermally synthesize SnO_2 and SnO_2/In_2S_3, and the SnO_2/In_2S_3 heterojunction material is cast-coated on a fluorine-doped tin oxide (FTO) electrode to form a SnO_2/In_2S_3/FTO photoanode. CeO_2 nanocubes are synthesized by a hydrothermal method and calcination. The CeO_2 surfaces are aminated by 3-aminopropyltriethoxysilane (APTES) treatment, and then HRP and Ab_2 are tethered through amide bonds after 1-ethyl-3-(3-dimethylaminopropyl) carbodiimide (EDC)/*N*-hydroxysuccinimide (NHS) activation. An HRP–CeO_2–Ab_2–bovine serum albumin (BSA) immune-complex is prepared after blocking the nonspecific sites of HRP–CeO_2–Ab_2 with BSA. The first antibody (Ab_1) is immobilized on the SnO_2/In_2S_3/FTO photoanode after chitosan (CS) coating and the Schiff base reactions of glutaraldehyde (GLD) with CS and Ab_1. After blocking the nonspecific sites with BSA, Ag (*i.e.* AFP) is immunologically immobilized, and then the HRP–CeO_2–Ab_2–BSA immune-complex is also immunologically linked to Ag. The labeled HRP and CeO_2 can catalyze the oxidation of 3-amino-9-ethylcarbazole (AEC) by H_2O_2 to generate a precipitate on the photoanode surface and thus attenuate the photocurrent, and thus, the sensitive PEC detection of AFP is achieved. The photocurrent linearly decreases with the increase in the logarithm of AFP concentration, with a limit of detection (LOD, S/N = 3) of 0.15 pg mL^{-1}.

Experimental

Preparation of the SnO_2/In_2S_3/FTO electrode

First, SnO_2 nanoparticles were synthesized as described in a previous report,[24] with minor modifications. Briefly, 0.471 g $SnCl_4{\cdot}5H_2O$ was dissolved in 30 mL of ultrapure water under stirring. After 15 min, 0.452 g NaOH was added, and then stirred for another 15 min, and 10 mL of 17.6 mg mL^{-1} citric acid (CA) was added. After cooling to room temperature, the white precipitate was collected by centrifugation and subsequently washed several times with ultrapure water and ethanol. After drying overnight in an oven at 60 °C, white SnO_2 nanoparticles were obtained.

Second, the SnO_2/In_2S_3 heterojunction material was synthesized by a facile one-pot method, as shown in Scheme 1A. 0.1000 g of the synthesized SnO_2 nanoparticles were sonicated and dispersed in 70 mL of ultrapure water, followed by adding 0.1408 g of $InCl_3{\cdot}4H_2O$ and 0.1163 g of L-cysteine (L-Cys). The dispersion was transferred to a 100 mL high-pressure reactor and reacted in an oven at 180 °C for 12 h. After cooling to room temperature, earthy yellow SnO_2/In_2S_3 was collected by centrifugation and washed alternately with ultrapure water and ethanol several times, and then dried overnight in an oven at 60 °C. In addition, different SnO_2/In_2S_3 mass ratios were examined by changing the mass of SnO_2 (optimized to be 0.1 g SnO_2) while other synthesis conditions remained constant. The dispersant is ultrapure water.

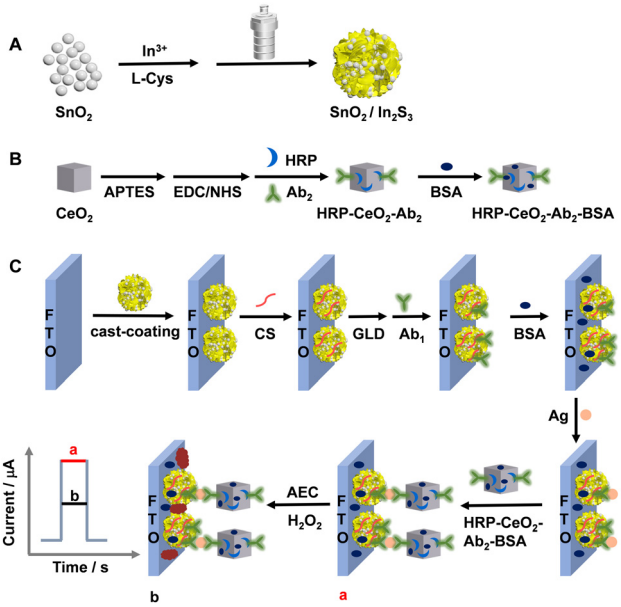

Scheme 1 Schematic for preparing the SnO_2/In_2S_3 heterojunction (A), the HRP–CeO_2–Ab_2–BSA complex (B), and the immune-photoelectrode (C).

Finally, the SnO_2/In_2S_3/FTO electrode was prepared by casting 20.0 μL of 2.00 mg mL^{-1} SnO_2/In_2S_3 suspension on the surface of a FTO electrode with an effective area of 0.250 cm^2, and then dried in a 60 °C oven.

Preparation of the HRP–CeO_2–Ab_2–BSA complex

CeO_2 nanocubes were prepared according to a previous report,[25] with minor modifications. In brief, 0.87 g $Ce(NO_3)_3{\cdot}6H_2O$ was dissolved in 40 mL of 6 M NaOH aqueous solution under stirring. After 30 min, the solution was transferred to a 100 mL autoclave and reacted in an oven at 180 °C for 24 h. After cooling to room temperature, the precipitate was collected by centrifugation and washed alternately with ultrapure water and ethanol several times, followed by drying overnight in an oven at 60 °C. Finally, the prepared precursor was calcined in a muffle furnace at 450 °C for 3 h, and CeO_2 powder was obtained after grinding.

Amino-functionalized CeO_2 (NH_2–CeO_2) was synthesized. 200 μL APTES was dispersed in 20 mL ethanol, and the pH was adjusted to 7.0 with 3 M HCl. Afterwards, 0.5 g CeO_2 was added and the dispersion was continuously stirred for 14 h. After centrifuging and washing with anhydrous ethanol three times and drying, NH_2–CeO_2 was obtained.

The HRP–CeO_2–Ab_2–BSA complex was prepared as shown in Scheme 1B. 10 mg EDC and 5 mg NHS were added in 1 mL of 100 μg mL^{-1} Ab_1 containing 2 mg mL^{-1} HRP. After

gently shaking at 4 °C for 2 h, the carboxyl groups on HRP and Ab_1 were activated. Afterwards, 2 mg mL^{-1} well-dispersed NH_2–CeO_2 was added into the mixture, and the amidation reaction occurred for 2 h. Then, the HRP–CeO_2–Ab_2 complex was obtained after centrifugation and washing with 0.01 M phosphate buffer solution (PBS) three times. To hinder nonspecific adsorption, HRP–CeO_2–Ab_2 was dispersed in 1 mL of 0.01 M PBS containing 300 μL 1% BSA. After gently shaking at 4 °C for 1 h, centrifuging, washing three times with 0.01 M PBS and then redispersing in 1 mL of 0.01 M PBS, the HRP–CeO_2–Ab_2–BSA complex was prepared. The dispersion was stored at 4 °C before use.

Preparation of the immune-electrode

The preparation process of the immune electrode is shown in Scheme 1C. 10 μL of 1% acetic acid solution containing 0.05% CS was added dropwise on the SnO_2/In_2S_3/FTO electrode. After natural drying at room temperature, 20 μL of 1% GLD was added to the electrode surface to trigger a cross-linking reaction between the CS amino groups and GLD aldehyde groups. After incubation for 30 min, the electrode was rinsed with ultrapure water to remove physically adsorbed GLD. Then, 20 μL of 10 μg mL^{-1} Ab_1 was added on the surface of the electrode and incubated overnight in a refrigerator at 4 °C. After washing away unbound Ab_1 with 0.01 M PBS (pH 7.40), 10 μL of 1% BSA was added dropwise, followed by incubation for 1 h to block nonspecific adsorption sites. After washing with 0.01 M PBS, 20 μL Ag at different concentrations were dropped onto the electrode and incubated at 4 °C for 1 h. Then, an Ag–Ab_1 complex was formed through the specific recognition of the antigen and antibody. After washing with 0.01 M PBS, 20 μL HRP–CeO_2–Ab_2–BSA dispersion was added dropwise to the electrode surface and incubated at 4 °C for 1 h. The prepared HRP–CeO_2–Ab_2–BSA/Ag/BSA/Ab_1/GLD/CS/SnO_2/In_2S_3/FTO electrode was washed and stored at 4 °C before use.

PEC immunoassay

The HRP–CeO_2–Ab_2–BSA/Ag/BSA/Ab_1/GLD/CS/SnO_2/In_2S_3/FTO electrode was placed in 10 mL 0.01 M PBS containing 5 mM AEC and 10 mM H_2O_2 for 30 min reaction at room temperature, and the HRP and CeO_2 catalyzed oxidation of AEC by H_2O_2 led to the generation of a precipitate on the immune-electrode.

PEC detection was done in 0.1 M PBS (pH 7.40) containing 0.05 M ascorbic acid (AA) at a bias of 0.05 V *vs.* SCE. The PEC detection was performed with a 100 mW cm^{-2} visible light source, with the light source switched on and off every 10 s.

Results and discussion

Characterization of the substrate electrode and materials

First, SnO_2, In_2S_3 and SnO_2/In_2S_3 were characterized by X-ray diffraction (XRD) and X-ray photoelectron spectroscopy (XPS), as shown in Fig. S1.† The XRD peaks at 26.6°, 33.9°, 37.9° and 51.8° are attributed to the (110), (101), (200) and (211) crystal planes of the SnO_2 tetragonal crystal structure (JCPDS No. 41-1115), respectively.[26] The XRD peaks at 27.4°, 33.2°, 43.6° and 47.7° are attributed to the (109), (0012), (1015) and (2212) crystal planes of pure tetragonal β-In_2S_3 (JCPDS No. 25-0390), respectively.[27] The characteristic XRD peaks of SnO_2 and In_2S_3 appeared in the SnO_2/In_2S_3 composite, and no impurity peaks were observed. The XPS results indicate the presence of Sn, O, In and S elements in the SnO_2/In_2S_3 composite. The two typical XPS peaks centered at 496.0 eV and 487.5 eV are ascribed to Sn $3d_{3/2}$ and Sn $3d_{5/2}$ of Sn(IV), respectively.[28] The XPS peak at 532.2 eV corresponds to chemisorbed oxygen on the SnO_2 surface and the peak at 532.8 eV is attributed to lattice oxygen (O–Sn) of SnO_2.[29] The peaks at 452.6 eV and 444.9 eV are attributed to In $3d_{3/2}$ and In $3d_{5/2}$ of In^{3+}, respectively.[30] The S 2p spectrum shows the addition of two XPS peaks of S $2p_{5/2}$ at 162.6 eV and S $2p_{1/2}$ at 161.5 eV.[31]

Second, the FTO-supported SnO_2, In_2S_3 and SnO_2/In_2S_3 were characterized by scanning electron microscopy (SEM) and energy dispersive X-ray spectroscopy (EDS), as shown in Fig. 1. The SnO_2 consists of irregular particles, while the In_2S_3 shows a flower-like microsphere structure composed of a large number of nanosheets. The SEM image of the SnO_2/In_2S_3 heterojunction displays the deposition of particulate SnO_2 on the In_2S_3 surface. The EDS pattern of SnO_2/In_2S_3/FTO and the revealed quantitative percentages of O, Sn, In, and S (inset in panel D) demonstrate that the SnO_2/In_2S_3 material was successfully synthesized by the one-pot method.

Third, bare FTO, SnO_2/FTO, In_2S_3/FTO and SnO_2/In_2S_3/FTO electrodes were characterized by cyclic voltammetry (CV) and electrochemical impedance spectroscopy (EIS) in 0.1 M PBS (pH 7.40) containing 2.0 mM $K_4[Fe(CN)_6]$ and 0.1 M Na_2SO_4, as shown in Fig. S2A and B.† The cleaned FTO electrode shows a pair of redox peaks with a peak-to-peak separation (ΔE_p) of 106 mV and a charge transfer resistance (R_{ct}) of 0.115 kΩ, verifying the well reversible electrode

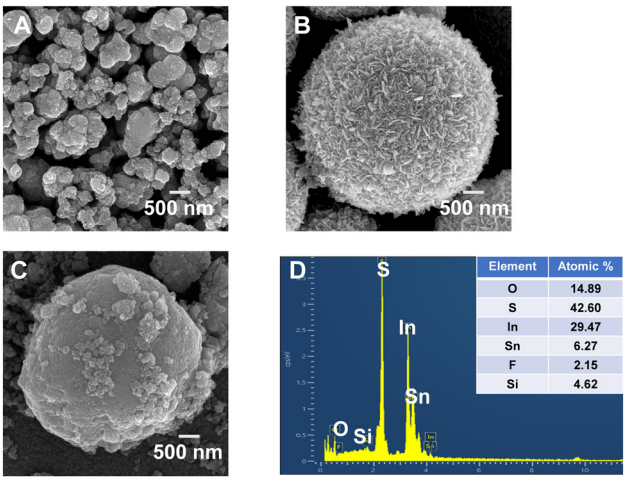

Fig. 1 SEM images of (A) SnO_2/FTO, (B) In_2S_3/FTO and (C) SnO_2/In_2S_3/FTO. (D) EDS spectrum of SnO_2/In_2S_3/FTO.

process of $Fe(CN)_6^{3-}/Fe(CN)_6^{4-}$ on the bare FTO electrode. The ΔE_p values obey the order 126 mV (In_2S_3/FTO) < 138 mV (SnO_2/FTO) < 151 mV (SnO_2/In_2S_3/FTO), and the R_{ct} values follow the order 0.303 kΩ (In_2S_3/FTO) < 0.594 kΩ (SnO_2/FTO) < 0.952 kΩ (SnO_2/In_2S_3/FTO). These results reasonably indicate the sequentially increased blocking of the electron transfer between solution-state $Fe(CN)_6^{3-}/Fe(CN)_6^{4-}$ and the electrode surface by the electrode-surface modification. The PEC performance of the FTO, SnO_2/FTO, In_2S_3/FTO and SnO_2/In_2S_3/FTO electrodes was characterized at 0.05 V in 0.1 M PBS (pH 7.40) containing 0.05 M AA, as shown in Fig. S2C.† The SnO_2/In_2S_3/FTO electrode shows a photocurrent notably larger than those of In_2S_3/FTO and SnO_2/FTO, indicating that the formation of a SnO_2/In_2S_3 heterojunction can improve the separation and transfer of photogenerated charges. As shown in Fig. S2D,† the photocurrent of the SnO_2/In_2S_3/FTO photoanode barely attenuated after switching on/off the light for ten cycles, indicating that the electrode has good stability.

Finally, as shown in Fig. S3,† UV-vis DRS and Mott–Schottky experiments were carried out to estimate the energy band structure of the material and discuss the possible charge transfer pathways of the SnO_2/In_2S_3 heterojunction (Scheme 2). Fig. S3A† shows the ultraviolet absorption edge of SnO_2 at 358 nm[32] and that of In_2S_3 at 650 nm.[33] Notably, after the formation of the SnO_2/In_2S_3 heterojunction, the absorption band is obviously red-shifted compared with those of the individual materials. Meanwhile, the enhanced visible light absorption is beneficial to improve the optoelectronic performance of the heterojunction. Both SnO_2 and In_2S_3 are direct bandgap semiconductors.[34,35] Therefore, in Fig. S3B and C,† according to the plots of $(\alpha h\nu)^2$ *versus* photon energy ($h\nu$), the band gaps of SnO_2 and In_2S_3 are estimated to be 3.7 eV and 2.1 eV, respectively, which are consistent with literature values.[36,37] The Mott–Schottky curves of both SnO_2 and In_2S_3 exhibit positive slopes, indicating that SnO_2 and In_2S_3 exhibit n-type semiconductor characteristics. In Mott–Schottky plots, the flat band potential (E_f) of n-type semiconductors is equivalent to the conduction band level (E_{CB}).[38] Therefore, the E_{CB} of SnO_2 and In_2S_3 is −0.63 V (*vs.* SCE) and −0.75 V (*vs.* SCE), respectively (Fig. S3D and E†). Then, according to the conversion relationship $E_g = E_{VB} - E_{CB}$, the E_{VB} of SnO_2 and In_2S_3 is estimated as 3.07 V (*vs.* SCE) and 1.35 V (*vs.* SCE), respectively. Finally, according to $E_{RHE} = E_{SCE} + 0.0591$ pH + 0.2415, the E_{CB} of SnO_2 and In_2S_3 is 0.05 V (*vs.* RHE) and −0.07 V (*vs.* RHE), and the E_{VB} of SnO_2 and In_2S_3 is 3.75 V (*vs.* RHE) and 2.03 V (*vs.* RHE), respectively, which agree well with literature results.[27,39]

Due to the matching of the energy band structures of SnO_2 and In_2S_3, the combination of SnO_2 and In_2S_3 can form a heterojunction that is beneficial to the separation and transfer of photogenerated charges and greatly improves the PEC performance. The possible charge transfer mechanism of this system is shown in Scheme 2. When the energy provided by the external light source with a visible light filter (400–700 nm) slightly excites SnO_2 and notably excites In_2S_3, electron–hole pair separation occurs in/on SnO_2 and especially In_2S_3. Subsequently, at the SnO_2/In_2S_3/FTO electrode, the photogenerated electrons are transferred from the relatively negative CB of In_2S_3 to the CB of SnO_2, and the holes are somewhat transferred from the relatively positive VB of SnO_2 to the VB of In_2S_3. Anyway, the electron transfer from In_2S_3 to SnO_2 should be obvious in the SnO_2/In_2S_3 heterojunction, though SnO_2 itself can only be slightly photoexcited by the filtered visible light to give a minor photocurrent and thus the hole transfer from SnO_2 to In_2S_3 is insignificant, probably leading to the formation of a special type-II heterojunction with notably unequal electron and hole flows. In fact, a conventional type-II heterojunction usually has comparable electron and hole flows (but not definitely strictly symmetric electron and hole flows in our opinion, due to the two different employed semiconductors with different photoelectric conversion efficiencies and with different CB-to-CB and VB-to-VB spacing). The successful construction of the heterojunction reduces the recombination degree of electron–hole pairs and improves the photocurrent response. When CP occurs on the SnO_2/In_2S_3/FTO electrode to prevent AA from approaching the FTO and In_2S_3 surfaces, the photocurrent will be decreased for signaling, as discussed in detail later. In summary, the above characterizations with XRD, XPS, SEM, EDS, CV, EIS, PEC detection, UV-vis DRS and Mott–Schottky curves have verified the involved materials and electrodes and the construction of the SnO_2/In_2S_3 heterojunction.

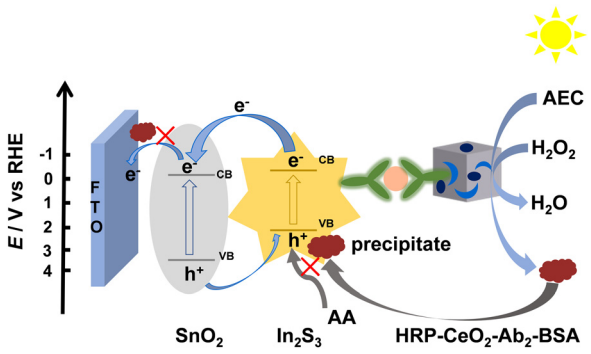

Scheme 2 Schematic of the possible charge transfer pathways of the SnO_2/In_2S_3 heterojunction and the PEC immune-sensing principle.

Characterization of the immune-complex and immune-electrode

The structural and elemental information of the carrier CeO_2 was studied with SEM, EDS, XRD, and Fourier transform infrared (FT-IR) spectra (Fig. S4†). CeO_2 shows a cubic shape with a *ca.* 200 nm size. The EDS analysis of CeO_2/FTO confirms the presence and a reasonable composition of Ce and O elements. The XRD peaks at 28.5°, 33.1°, 47.5° and 56.3° are attributed to the (111), (200), (220) and (311) crystal planes of CeO_2 (JCPDS No. 065-5923), respectively, verifying the successful preparation of CeO_2.[40] The characteristic absorption peaks near 3100 cm^{-1} and

1630 cm^{-1} of NH_2–CeO_2 in the FT-IR spectrum are stretching vibration peaks and bending vibration peaks of N–H, respectively, confirming the successful surface amination of CeO_2 nanocubes.

Ultraviolet-visible (UV-vis) absorption spectra were used to verify that HRP and Ab_2 were successfully modified on NH_2–CeO_2, as shown in Fig. S4E.† The characteristic absorption peak of NH_2–CeO_2 is found at *ca.* 300 nm. Ab_2 exhibits its characteristic absorption peak near 280 nm.[41] HRP as a protein has a typical protein absorption peak at *ca.* 270 nm. The absorption peak near 270–280 nm in HRP–CeO_2–Ab_2 becomes larger. These results validate the successful preparation of HRP–CeO_2–Ab_2.

Scheme 1C illustrates the modification steps of the immune-sensing electrodes. First, CV and EIS were used to characterize each modification step of the immune-electrode in 0.1 M PBS (pH 7.40) containing 2.0 mM K_4-$Fe(CN)_6$ and 0.1 M Na_2SO_4, as shown in Fig. 2A and B. With step-by-step modifications, the ΔE_p and R_{ct} values increase as follows: SnO_2/In_2S_3/FTO (151 mV, 0.952 kΩ) < GLD/CS/SnO_2/In_2S_3/FTO (172 mV, 1.38 kΩ) < Ab_1/GLD/CS/SnO_2/In_2S_3/FTO (187 mV, 1.58 kΩ) < BSA/Ab_1/GLD/CS/SnO_2/In_2S_3/FTO (194 mV, 1.92 kΩ) < Ag/BSA/Ab_1/GLD/CS/SnO_2/In_2S_3/FTO (211 mV, 2.23 kΩ) < HRP–CeO_2–Ab_2–BSA/Ag/BSA/Ab_1/GLD/CS/SnO_2/In_2S_3/FTO (229 mV, 2.84 kΩ) before CP < HRP–CeO_2–Ab_2–BSA/Ag/BSA/Ab_1/GLD/CS/SnO_2/In_2S_3/FTO after CP (252 mV, 3.83 kΩ). These results reasonably indicate the decrease in the electrode activity after modifying an electron-insulating material and confirm the successful stepwise construction of the immune-electrode.

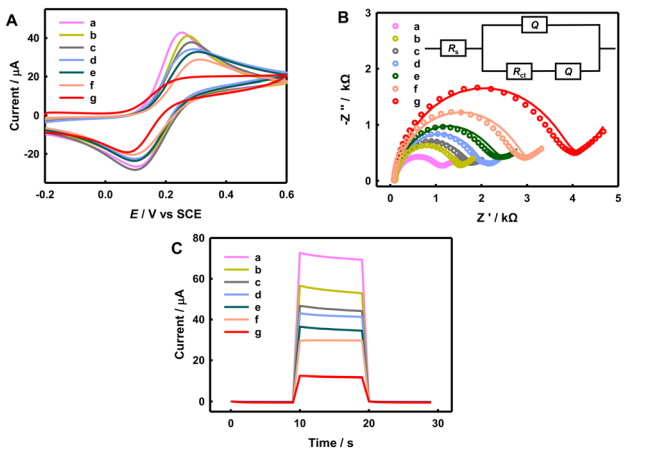

Fig. 2 (A) CV curves, (B) EIS spectra and (C) photocurrent responses of (a) SnO_2/In_2S_3/FTO, (b) GLD/CS/SnO_2/In_2S_3/FTO, (c) Ab_1/GLD/CS/SnO_2/In_2S_3/FTO, (d) BSA/Ag/BSA/Ab_1/GLD/CS/SnO_2/In_2S_3/FTO, (e) Ag/BSA/Ab_1/GLD/CS/SnO_2/In_2S_3/FTO, and HRP–CeO_2–Ab_2–BSA/Ag/BSA/Ab_1/GLD/CS/SnO_2/In_2S_3/FTO (f) before and (g) after CP. CV scan rate: 50 mV s^{-1}. EIS experiment: 100 kHz–0.01 Hz, 0.20 V, 200 s resting time, circles: experimental values; curve: fitted to the modified Randles equivalent circuit (inset). Photocurrent experiment: 0.1 M PBS (pH 7.40) containing 0.05 M AA at 0.05 V *vs.* SCE. 500 pg mL^{-1} Ag.

Photocurrents of the immune-electrodes at different fabrication steps were measured at 0.05 V in 0.1 M PBS (pH 7.40) containing 0.05 M AA, as shown in Fig. 2C. The photocurrent values follow the order 70 μA (SnO_2/In_2S_3/FTO) > 55 μA (GLD/CS/SnO_2/In_2S_3/FTO) > 46 μA (Ab_1/GLD/CS/SnO_2/In_2S_3/FTO) > 42 μA (BSA/Ab_1/GLD/CS/SnO_2/In_2S_3/FTO) > 36 μA (Ag/BSA/Ab_1/GLD/CS/SnO_2/In_2S_3/FTO), because the surface modifications of GLD/CS, Ab_1, BSA and Ag (AFP) on the electrode can hinder the mass transfer and electron transfer of the hole scavenger AA. After the HRP–CeO_2–Ab_2–BSA labeling of the captured AFP, the photocurrent of HRP–CeO_2–Ab_2–BSA/Ag/BSA/Ab_1/GLD/CS/SnO_2/In_2S_3/FTO further decreased to 30 μA, due to the further increased steric hindrance effect. CeO_2 and HRP are capable of catalyzing the oxidation of AEC by H_2O_2 to produce a red precipitate, and the precipitation of the insoluble precipitate on the electrode and semiconductor surface can further quench the photocurrent (Scheme 2). As a result, after CP on the immune-electrode, the photocurrent of the immune-electrode decreased significantly to 12 μA because the insoluble precipitate notably prevents the transfer of electron donors to the electrode surface. In summary, both HRP–CeO_2–Ab_2–BSA and the generated red precipitate can decrease the photocurrent of the immune-electrode, enabling the construction of a signal-off immune-sensor for the sensitive PEC detection of AFP.

PEC immune-sensing performance

In order to achieve the best PEC performance, we studied the optimization of several experimental parameters, as shown and discussed in Fig. S5.† The optimal mass of SnO_2 is 0.1 g. The experimental conditions of the CP by CeO_2 and HRP were also optimized. The optimal bias is 0.05 V *vs.* SCE, the optimal AA concentration is 0.05 M, the optimal AEC concentration is 5 mM, the optimal H_2O_2 concentration is 10 mM, and the optimal reaction time is 30 min.

Under the optimal conditions, the photocurrent of the PEC immune-electrode decreases with the increase in AFP concentration, due to the CP effect (Fig. 3). The photocurrent has a linear relationship with the common logarithm of AFP concentration from 500 fg mL^{-1} to 50 ng mL^{-1}, with a linear regression equation of $I = -4.23 \lg c_{Ag} + 10.5$ ($R^2 = 0.997$) and

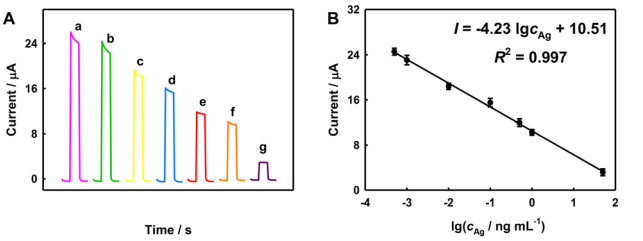

Fig. 3 (A) Photocurrent responses to AFP at different concentrations (a–g: 500 fg mL^{-1}, 1 pg mL^{-1}, 10 pg mL^{-1}, 100 pg mL^{-1}, 500 pg mL^{-1}, 1 ng mL^{-1}, 50 ng mL^{-1}). (B) Corresponding calibration curve, n = 3.

a LOD of 0.15 pg mL^{-1} (S/N = 3). The analytical performance of the PEC immune-electrode is better than many reported results, as listed in Table S1.†

The stability, reproducibility and selectivity of the immune-electrode were investigated, as shown in Fig. S6.† The immune-electrode still has good stability after 200 s cycling. Five immune-electrodes were prepared in parallel to detect 500 pg mL^{-1} AFP, and the relative standard deviation (RSD) was 8.4%, indicating good reproducibility. In comparison with those to IgG, CEA, CYFRA21-1 and PCT (each at 50 ng mL^{-1}, see ESI† for their full names), the photocurrent response to 500 pg mL^{-1} AFP was the most obvious. Hence, this immunosensor has good stability, reproducibility and selectivity.

We detected AFP in serum samples from healthy people using this immunosensor and the standard addition method. As listed in Table S2,† the recovery (92.0–106%) and RSD (3.3–7.6%) results are acceptable, suggesting that the PEC immunoassay has the potential to detect AFP in actual samples.

Conclusion

In conclusion, a novel signal-off immune-sensing PEC method for AFP assay has been investigated. The immune-sensor consisted of a SnO_2/In_2S_3 heterojunction as a substrate photoanode material to amplify the photocurrent and HRP–CeO_2–BSA as a Ab_2-labeled complex to quench the photocurrent due to the CP effect. Compared with those of In_2S_3/FTO and SnO_2/FTO, SnO_2/In_2S_3/FTO showed superior PEC performance. The labelled CeO_2 and HRP can catalyze the oxidation of AEC to produce a precipitate on the electrode surface to reduce the photocurrent. Under the optimized conditions, the PEC immunosensor displayed high sensitivity, low LOD, high selectivity, and potential in actual sample analysis. However, the actual operation process of the immunosensor is not so facile, and some biologically active substances such as antigens and enzymes have relatively high requirements for storage and experimental operation environments. Anyway, the suggested strategy of simultaneously using a natural enzyme and nanozyme may inspire the further innovation of PEC analysis strategies.

Author contributions

Lu Li: investigation, data curation, and writing – original draft. Yaqing Weng: resources. Chenglong Sun: data curation and software. Yueyi Peng: writing – review, and funding acquisition. Qingji Xie: writing – review & editing, project administration, and funding acquisition.

Conflicts of interest

The authors declare that they have no known competing financial interests or personal relationships that could have appeared to influence the work reported in this paper.

Acknowledgements

The authors gratefully acknowledge the financial support from the National Science Foundation of China (22074039, 21675050, 22002042) and the Changsha Municipal Natural Science Foundation (kq2007006).

References

1 K. Lu, C. Liu, G. Wang, W. Yang, K. Fan, S. Lazarouk, V. Labunov, L. Dong, D. Li and X. Yang, *Biomater. Sci.*, 2022, **10**, 3823–3830.
2 H. Sung, J. Ferlay, R. L. Siegel, M. Laversanne, I. Soerjomataram, A. Jemal and F. Bray, *Ca-Cancer J. Clin.*, 2021, **71**, 209–249.
3 Y. Wu, H. Su, J. Yang, Z. Wang, D. Li, H. Sun, X. Guo and S. Yin, *J. Colloid Interface Sci.*, 2020, **580**, 583–591.
4 D. Zheng, Z. Zheng, J. Yang, Y. Xu, K.-M. Ng, L. Huang, Y. Chen and W. Gao, *Microchem. J.*, 2022, **181**, 107779.
5 X. Liang, Z. Lin, L. Li, D. Tang and J. Kong, *Analyst*, 2022, **147**, 2851–2858.
6 W. Zhang, D. Han, Z. Wu, K. Yang, S. Sun and J. Wen, *Sens. Actuators, B*, 2022, 133004.
7 P. Chen, P. Jiang, Q. Lin, X. Zeng, T. Liu, M. Li, Y. Yuan, S. Song, J. Zhang, J. Huang, B. Ying and J. Chen, *ACS Appl. Mater. Interfaces*, 2022, **14**, 28697–28705.
8 J. Guo, J. Wang, Z. Wang, S. Li and J. Wang, *Biosens. Bioelectron.*, 2022, **218**, 114766.
9 J. Shi, Z. Chen, C. Zhao, M. Shen, H. Li, S. Zhang and Z. Zhang, *Coord. Chem. Rev.*, 2022, **469**, 214675.
10 Z. Li, J. Lu, W. Wei, M. Tao, Z. Wang and Z. Dai, *Chem. Commun.*, 2022, **58**, 12418–12430.
11 L. Li, H. Yang, L. Li, X. Tan, S. Ge, L. Zhang, J. Yu and Y. Zhang, *ACS Sens.*, 2022, **7**, 2429–2437.
12 C. V. Reddy, R. R. Kakarla, J. Shim, R. R. Zairov and T. M. Aminabhavi, *Environ. Res.*, 2022, 114672.
13 N. Zhang, Y. Li, G. Zhao, J. Feng, Y. Li, Y. Wang, D. Zhang and Q. Wei, *Talanta*, 2023, **253**, 124048.
14 Q. Liu, H. Zhang, H. Jiang, P. Yang, L. Luo, Q. Niu and T. You, *Biosens. Bioelectron.*, 2022, **216**, 114634.
15 J. Zhang, R. Balasubramanian and X. Yang, *Chem. Eng. J.*, 2023, **453**, 139776.
16 T. Xu, X. Su, Y. Zhu, S. Khan, D.-L. Chen, C. Guo, J. Ning, Y. Zhong and Y. Hu, *J. Colloid Interface Sci.*, 2023, **629**, 1027–1038.
17 Q. Gao, C. Cao, J. Ao, J. Bi, L. Yao, J. Guo, G. Sun, W. Liu, Y. Zhang, F. Liu and W. Li, *Appl. Surf. Sci.*, 2022, **578**, 152063.
18 C.-J. Li, J. Hu, G. Gao, J.-H. Chen, C.-S. Wang, H. Zhou, G. Chen, P. Qu, P. Lin and W.-W. Zhao, *Adv. Funct. Mater.*, 2023, **33**, 2211277.
19 G.-Q. Wang, J.-J. Wei, J.-Y. Ye, A.-J. Wang, L.-P. Mei and J.-J. Feng, *Sens. Actuators, B*, 2023, **381**, 133421.
20 L. Li, X. Zheng, Y. Huang, L. Zhang, K. Cui, Y. Zhang and J. Yu, *Anal. Chem.*, 2018, **90**, 13882–13890.
21 W.-W. Zhao, Z.-Y. Ma, P.-P. Yu, X.-Y. Dong, J.-J. Xu and H.-Y. Chen, *Anal. Chem.*, 2012, **84**, 917–923.

22 X. Huang, Q. Lin, L. Lu, M. Li and D. Tang, *Anal. Chim. Acta*, 2022, **1228**, 340358.
23 G. Xiao, H. Li, Y. Zhao, H. Wei, J. Li and H. Su, *ACS Appl. Nano Mater.*, 2022, **5**, 14147–14170.
24 M. A. Tekalgne, A. Hasani, D. Y. Heo, Q. Van Le, T. P. Nguyen, T. H. Lee, S. H. Ahn, H. W. Jang and S. Y. Kim, *J. Phys. Chem. C*, 2020, **124**, 647–652.
25 M. Li, W. Liang, R. Yuan and Y. Chai, *ACS Appl. Mater. Interfaces*, 2019, **11**, 11834–11840.
26 M. C. Shibu, M. D. Benoy, S. Shanavas, J. Duraimurugan, G. Suresh Kumar, M. Abu Haija, P. Maadeswaran, T. Ahamad, Q. Van Le and S. M. Alshehri, *Chemosphere*, 2022, **307**, 136105.
27 H. Qiu, S. Fang, G. Huang and J. Bi, *Environ. Res.*, 2020, **190**, 110018.
28 H. Yang, C. Nan, N. Gao, W. Zhou, F. Gao, D. Dong, D. Dou, Y. Liu, Z. Liang and D. Yang, *Electrochim. Acta*, 2022, **430**, 141086.
29 X.-Q. Qiao, Z.-W. Zhang, D.-F. Hou, D.-S. Li, Y. Liu, Y.-Q. Lan, J. Zhang, P. Feng and X. Bu, *ACS Sustainable Chem. Eng.*, 2018, **6**, 12375–12384.
30 Z. He, M. S. Siddique, H. Yang, Y. Xia, J. Su, B. Tang, L. Wang, L. Kang and Z. Huang, *J. Cleaner Prod.*, 2022, **339**, 130634.
31 X. Wang, H. Li, J. Zhang, X. Liu and X. Zhang, *J. Alloys Compd.*, 2020, **831**, 154798.
32 W. Hu, N. D. Quang, S. Majumder, M. J. Jeong, J. H. Park, Y. J. Cho, S. B. Kim, K. Lee, D. Kim and H. S. Chang, *Appl. Surf. Sci.*, 2021, **560**, 149904.
33 Y. Li, R. Xu, D. Wei, R. Feng, D. Fan, N. Zhang and Q. Wei, *New J. Chem.*, 2020, **44**, 346–353.
34 W. Ren, J. Yang, W. Chen, J. Zhang, Y. Sun, Y. Zheng, H. Zhao and B. Liang, *Mater. Res. Bull.*, 2022, **153**, 111884.
35 C. Ding, J. Guo, P. Chen, W. Gan, Z. Yin, S. Qi, M. Zhang and Z. Sun, *Appl. Surf. Sci.*, 2022, **596**, 153629.
36 D. Fan, X. Liu, X. Shao, Y. Zhang, N. Zhang, X. Wang, Q. Wei and H. Ju, *Microchim. Acta*, 2020, **187**, 332.
37 H. Chai, L. Gao, P. Wang, F. Li, G. Hu and J. Jin, *Appl. Catal., B*, 2022, **305**, 121011.
38 X. Wang, Q. Lu, Y. Sun, K. Liu, J. Cui, C. Lu and H. Dai, *J. Environ. Chem. Eng.*, 2022, **10**, 108354.
39 M. Ismael, E. Elhaddad and M. Wark, *Colloids Surf., A*, 2022, **638**, 128288.
40 D. Sharma, V. R. Satsangi, R. Shrivastav, U. V. Waghmare and S. Dass, *Int. J. Hydrogen Energy*, 2016, **41**, 18339–18350.
41 X.-P. Liu, N. Chang, J.-S. Chen, C.-J. Mao and B.-K. Jin, *Microchem. J.*, 2021, **168**, 106337.